PAPER • OPEN ACCESS

Spin Nernst effect in a *p*-band semimetal InBi

View the article online for updates and enhancements.

New Journal of Physics

The open access journal at the forefront of physics

CrossMark

PAPER

Spin Nernst effect in a *p*-band semimetal InBi

Yang Zhang[1,2,3,4], Qiunan Xu[1,4], Klaus Koepernik[2], Chenguang Fu[1] , Johannes Gooth[1], Jeroen van den Brink[2], Claudia Felser[1] and Yan Sun[1,5]

1 Max Planck Institute for Chemical Physics of Solids, 01187 Dresden, Germany
2 Leibniz Institute for Solid State and Materials Research, 01069 Dresden, Germany
3 Department of Physics, Massachusetts Institute of Technology, Cambridge, Massachusetts 02139, United States of America
4 These two authors contributed equally.
5 Author to whom any correspondence should be addressed.

E-mail: ysun@cpfs.mpg.de

Abstract

Since spin currents can be generated, detected, and manipulated via the spin Hall effect (SHE), the design of strong SHE materials has become a focus in the field of spintronics. Because of the recent experimental progress also the spin Nernst effect (SNE), the thermoelectrical counterpart of the SHE, has attracted much interest. Empirically strong SHEs and SNEs are associated with *d*-band compounds, such as transition metals and their alloys—the largest spin Hall conductivity (SHC) in a *p*-band material is $\sim 450\ (\hbar/e)\ (\Omega\ \mathrm{cm})^{-1}$ for a Bi–Sb alloy, which is only about a fifth of platinum. This raises the question whether either the SHE and SNE are naturally suppressed in *p*-bands compounds, or favourable *p*-band systems were just not identified yet. Here we consider the *p*-band semimetal InBi, and predict it has a record SHC $\sigma_{xy}^{z} \approx 1100\ (\hbar/e)\ (\Omega\ \mathrm{cm})^{-1}$ which is due to the presence of nodal lines in its band structure. Also the spin-Nernst conductivity $\alpha_{zx}^{y} \approx 1.2\ (\hbar/e)(A/m \cdot K)$ is very large, but our analysis shows its origin is different as the maximum appears in a different tensor element compared to that in SHC. This insight gained on InBi provides guiding principles to obtain a strong SHE and SNE in *p*-band materials and establishes a more comprehensive understanding of the relationship between the SHE and SNE.

The joint utilisation of the spin and charge degree of freedom in solids is the main target of spintronics, in which the spin current generation, detection, and manipulation are the three crucial objectives [1–3]. The spin Hall effect (SHE) provides an effective technology to convert the charge current into a pure spin current, where an applied electric field can generate a transverse spin current with the spin polarization perpendicular to both the spin and charge currents [4–7]. Vice versa, the inverse SHE provides an effective method to manipulate the spin current without a magnetic field [5, 8]. Due to this versatility the SHE has attracted extensive interest in recent years, and much effort has been devoted to the theoretical understanding and engineering of strong SHE materials [6, 8–13].

In general the SHE has two distinct origins, an extrinsic contribution from the scattering and an intrinsic one from the band structure. The intrinsic part can be formulated via the spin Berry curvature (SBC) similar to the anomalous Hall effect [7, 14, 15]. Apart from the SHE, a transverse spin current can be generated by a temperature gradient instead of an electric field, which constitutes the spin Nernst effect (SNE) [16–18]. The SNE can also be formulated via the Kubo formula approach based on the electronic band structure [9, 10, 15, 19–24]. Thus the electronic band structure plays a crucial role in searching and designing strong SHE and SNE materials.

Though the precise reason is not clear to date, empirically materials with a strong SHE are primarily dominated by *d*-orbital-related compounds [7, 12, 13, 25, 26] such as 5*d*-transition metals and alloys. The spin Hall conductivity (SHC) or the spin Hall angle (SHA) in *p*-band compounds/alloys has been experimental measured in Bi_2Se_3 [27–29], $(Bi,Sb)_2Te_3$ [28, 30–32], and BiSb [33, 34]. And the largest SHC found in *p*-band materials is in a Bi–Sb alloy [35, 36] at around 450 $((\hbar/e)\ (\Omega\ \mathrm{cm})^{-1})$. Very recently, it was found that the nodal line band structure could generate strong SHCs because of the large local SBC

[37, 38]. Employing this guiding principle, we theoretically predict a large intrinsic SHC of about $1100\,((\hbar/e)\,(\Omega\,\text{cm})^{-1})$ in the p-band semimetal InBi. Substitution of the electric field by a temperature gradient, reveals a large spin Nernst conductivity (SNC) of about $1.2(\hbar/e)(A/m \cdot K)$ at 300 K. This shows that the SNE and SHE can be strongly enhanced by the topological band structure, and that the large SNC and SHC need not be intrinsically weak in cheaper and therefore commercially more attractive p-band materials. Though both the intrinsic SHE and SNE can be understood from the SBC, their largest value appears at different tensor elements, implying different origins.

To understand the effect of the nodal line band structure on the SHE and especially the SNE, we first consider two simple systems by effective model Hamiltonians. The 3D nodal line effective model around the Γ point is written in the form of

$$H_{\text{eff}}(\vec{k}) = \begin{pmatrix} H'(\vec{k}) & 0 \\ 0 & H'^{*}(\vec{k}) \end{pmatrix}$$

$$H(\vec{k}) = \varepsilon(\vec{k}) + d_i(\vec{k})\sigma_i + d_4\sigma_1$$

$$(1)$$

where σ_i are the Pauli matrices, $d_1 + id_2 + d_4 = A(k_x + ik_y) + Ck_z$, and $d_3 = M - B(k_x^2 + k_y^2 + k_z^2)$. In order to obtain a non-zero SNC, we break the balance of the SHC by reducing the symmetry:

$$H_{\text{eff}}(\vec{k}) = \begin{pmatrix} H'(\vec{k}) & 0 \\ 0 & H'^{*}(\vec{k}) \end{pmatrix}$$

$$H'(\vec{k}) = d_1'\sigma_1 + d_2'\sigma_2 + d_4'\sigma_1 \begin{pmatrix} M_1 - (B_1 k_x^2 + B_2 k_y^2 + B_3 k_z^2) & 0 \\ 0 & -[M_2 - (B_1' k_x^2 + B_2' k_y^2 + B_3' k_z^2)] \end{pmatrix}$$

$$(2)$$

where $d_1' + id_2' + d_4' = A_1 k_x + iA_2 k_y + Ck_z$. To perform the integral in the whole Brillouin zone (BZ), we projected the continuous $\vec{k} \cdot \vec{p}$ model to the lattice by the replacement of $k_i = (1/a)\sin(ak_i)$ and $k_i^2 = (2/a^2)(1 - \cos(ak_i))$ with lattice constant $a = 1$ Å

The SHC is calculated by the Kubo formula approach [7, 15]:

$$\sigma_{ij}^k = e\int_{\text{BZ}} \frac{d\vec{k}}{(2\pi)^3} \sum_n f_{n\vec{k}} \Omega_{n,ij}^{\text{SHE},k}(\vec{k}),$$

$$\Omega_{n,ij}^{\text{SHE},k}(\vec{k}) = -2\,\text{Im} \sum_{n' \neq n} \frac{\langle n\vec{k}|J_i^k|n'\vec{k}\rangle\langle n'\vec{k}|v_j|n\vec{k}\rangle}{(E_{n\vec{k}} - E_{n'\vec{k}})^2}$$
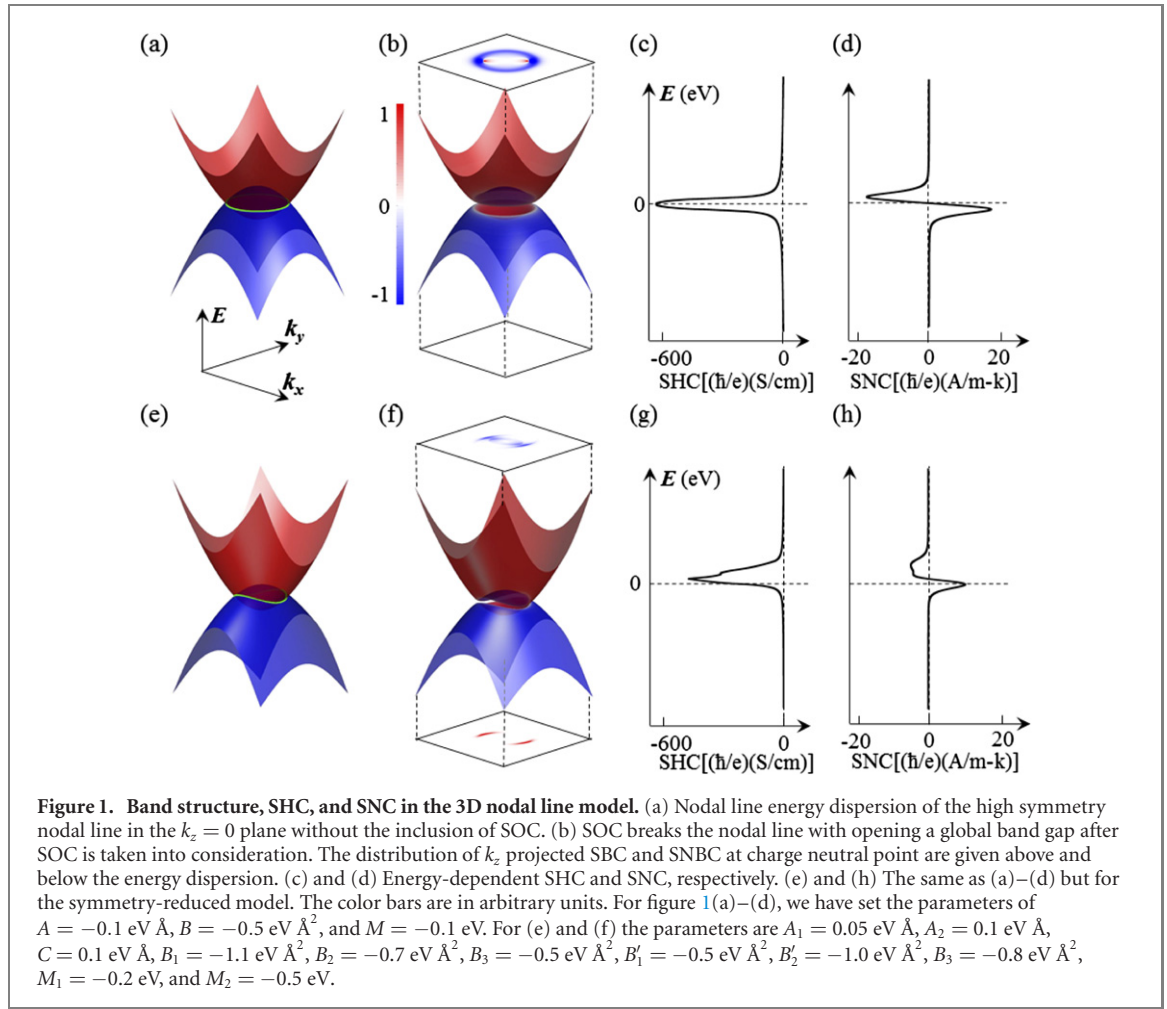
$$(3)$$

where $f_{n\vec{k}}$ is the Fermi–Dirac distribution for the nth band. $J_i^k = \frac{1}{2}\{v_i, s_k\}$ is the conventional spin current operator [39] with spin operator s, velocity operator v_i, and $i, j, k = x, y, z$. $|n\vec{k}\rangle$ is the eigenvector for the Hamiltonian H at eigenvalue $E_{n\vec{k}}$. $\Omega_{n,ij}^{\text{SHE},k}(\vec{k})$ is referred to as the SBC for the nth band. The SNC is calculated via [40, 41]

$$\alpha_{ij}^k = \frac{1}{T}\int_{\text{BZ}} \frac{d^3 k}{(2\pi)^3} \sum_n \Omega_{n,ij}^{\text{SNE},k}(\vec{k}).$$

$$(4)$$

A $500 \times 500 \times 500$ k-grid in the BZ was used for the integral of the SHC and SNC. For convenience, we call $\Omega_{n,ij}^{\text{SNE},k}(\vec{k}) = \Omega_{n,ij}^{S,k}(\vec{k})[(E_n - E_F)f_{n\vec{k}} + k_B T \ln(1 + e^{\frac{E_n - E_F}{-k_B T}})]$ the spin Nernst Berry curvature (SNBC).

Here we construct the 3D nodal line $k \cdot p$ model with a nodal line in $k_z = 0$ plane without SOC. As soon as SOC is taken into consideration, the linear crossing is gapped and leads to a SHC plateau in the band gap [37]. Though the SHC reaches the maximum value at the charge neutral point, the SHC is zero there because of the electron and hole symmetry. Comparing the SBC and SNBC distribution in reciprocal space, it is found that the SNBC is zero at any k-point, while the SBC has a strong hot ring from the nodal-line-like band anti-crossing (see figure 1(b)). From equation (2), one can find that the SNBC is actually a redistribution of the SBC because of the temperature effect, which should be cancelled out by the electron–hole symmetry. To break the electron–hole symmetry, we have reduced the symmetry of the effective model Hamiltonian, making the system non-insulating and tilting the nodal line. Meanwhile, a finite SNC appears at the charge neutral point. In figures 1(b) and (f), we also analyzed the SBC and SNBC distribution in the $k_x - k_y$ plane. Because of the dispersion of the nodal ring, the high intensity of the SBC changes from a hot ring to two hotspots, resulting in a non-zero SNBC, as presented in the lower panel of figure 1(f). By integrating the SNBC, one can obtain a non-zero SNC at the charge neutral point. Therefore, the non-zero SNC must break the balance of the SHC distribution in energy space.
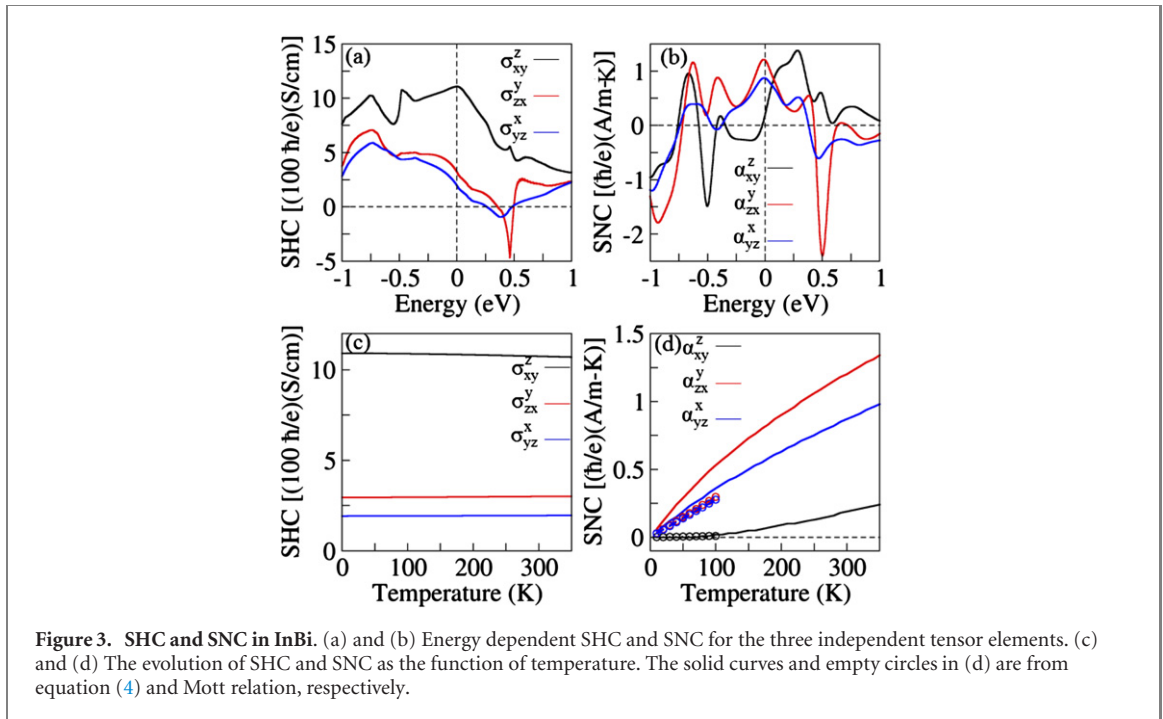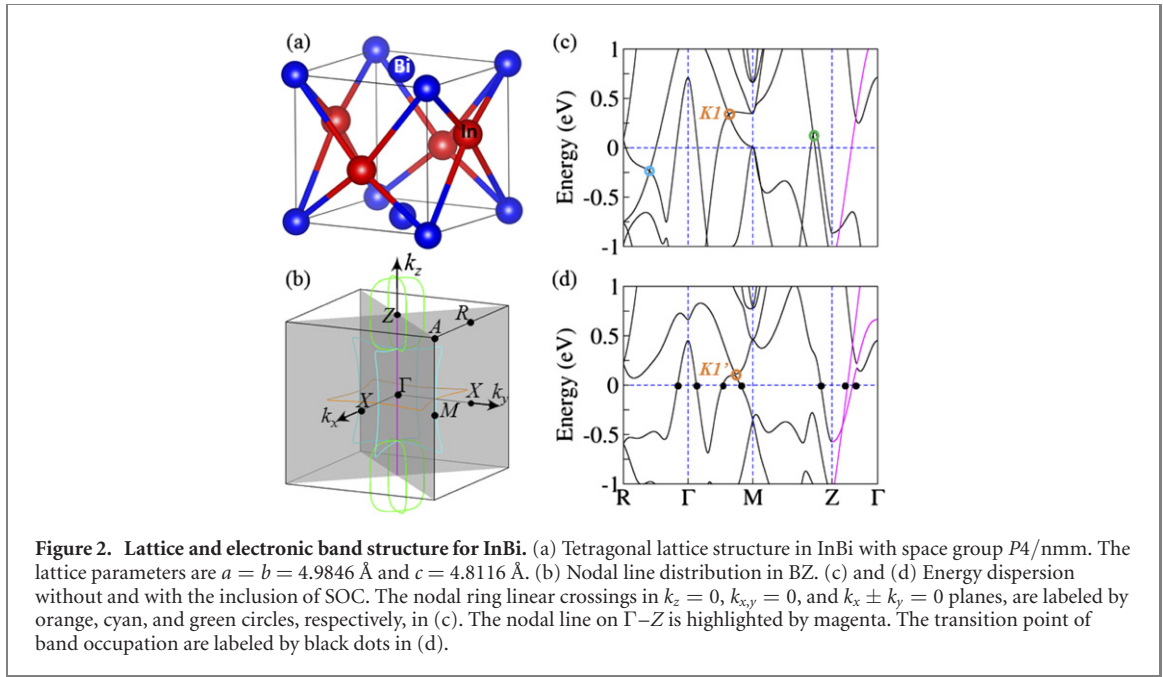
Then, we calculated the SHE and SNE for the real material of we employed the experimental lattice constants in all our calculations [42]. First-principles calculations were performed using the localized

Figure 1. **Band structure, SHC, and SNC in the 3D nodal line model.** (a) Nodal line energy dispersion of the high symmetry nodal line in the $k_z = 0$ plane without the inclusion of SOC. (b) SOC breaks the nodal line with opening a global band gap after SOC is taken into consideration. The distribution of k_z projected SBC and SNBC at charge neutral point are given above and below the energy dispersion. (c) and (d) Energy-dependent SHC and SNC, respectively. (e) and (h) The same as (a)–(d) but for the symmetry-reduced model. The color bars are in arbitrary units. For figure 1(a)–(d), we have set the parameters of $A = -0.1$ eV Å, $B = -0.5$ eV Å^2, and $M = -0.1$ eV. For (e) and (f) the parameters are $A_1 = 0.05$ eV Å, $A_2 = 0.1$ eV Å, $C = 0.1$ eV Å, $B_1 = -1.1$ eV Å^2, $B_2 = -0.7$ eV Å^2, $B_3 = -0.5$ eV Å^2, $B_1' = -0.5$ eV Å^2, $B_2' = -1.0$ eV Å^2, $B_3 = -0.8$ eV Å^2, $M_1 = -0.2$ eV, and $M_2 = -0.5$ eV.

atomic orbital basis and the full potential, as implemented in the full potential local orbital code (FPLO) [43]. Exchange and correlations are considered in the generalized gradient approximation, following the Perdew–Burke–Ernzerhof parametrization scheme [44]. In the DFT part, $1s$ to $3d$ orbitals of In are treated as semi-core states, and $4s, 4p, 5s, 4d, 5p, 6s, 5d, 6p$ are treated as valence states. For Bi, $1s$ to $4f$ are treated as semi-core states, and $5s, 5p, 6s, 5d, 6p, 7s, 6d, 7p$ are treated as valence states. Since we are using the atomic basis, a high-symmetry tight binding Hamiltonian is constructed via projecting the Bloch states onto a small local basis set (104 bands for 4 atoms) around Fermi level, which consists of $5s, 5p, 6s, 5d, 6p$ orbitals for In and $6s, 6p, 7s, 6d, 7p$ of Bi. The projected tight binding Hamiltonian perfectly reproduced the DFT band structures even at 10 eV away from Fermi level. A very fine k-mesh up to $500 \times 500 \times 500$ in the BZ is used for the integral of SHC and SNC.

InBi has a tetragonal structure with space group P4/nmm space group and weak bonding between the neighboring sublayer of Bismuth. The glide mirror symmetries $(m_{001}|1/2, 1/2, 0)$ and $(m_{010}|0, 1/2, 0)$ are crucial for the existence of nodal lines. Indeed, InBi has been reported to exhibit nonsymmorphic symmetry-protected nodal lines at the edge of the BZ [42]. However, these kinds of nodal lines are just band degeneracies from band folding between different BZs, thus does not exhibit any topological charge or SBC and, therefore, cannot generate the SHE and SNE [38]. In the current work, we find another type of nodal line inside the BZ protected by mirror symmetry and rotation symmetry, which generates a strong SHE and SNE. As shown in figure 2(b), there are four classes of nodal lines, located in the high-symmetry planes of $k_{x,y} = 0$, $k_z = 0$, and $k_x \pm k_y = 0$, and high-symmetry line of $\Gamma-Z$, respectively. Without including the SOC, the inverted bands have opposite mirror eigenvalues of 1 and -1, respectively, in the planes of $k_{x,y} = 0$, $k_z = 0$, and $k_x \pm k_y = 0$, leading to the double degenerated nodal lines. Along the high-symmetry line of $\Gamma-Z$, the double band degeneracy (highlighted by magenta in figure 2(c)) is due to the c_4^z rotation symmetry. The spin rotation symmetry is broken by SOC and the linear crossings are also gapped out, which is often accompanied by strong band entanglements and yields a large SBC.

The SHC and SNC are $3 \times 3 \times 3$ tensors, representing the spin current $\vec{J}_{si}^k$ generated by the electric field $\vec{E}$ via $\vec{J}_{si}^k = \sum_j \sigma_{ij}^k \vec{E}_j$ and temperature gradient ∇T by $\vec{J}_{si}^k = \sum_j \alpha_{ij}^k \nabla T_j$. There are only three independent

Figure 2. Lattice and electronic band structure for InBi. (a) Tetragonal lattice structure in InBi with space group $P4/nmm$. The lattice parameters are $a = b = 4.9846$ Å and $c = 4.8116$ Å. (b) Nodal line distribution in BZ. (c) and (d) Energy dispersion without and with the inclusion of SOC. The nodal ring linear crossings in $k_z = 0$, $k_{x,y} = 0$, and $k_x \pm k_y = 0$ planes, are labeled by orange, cyan, and green circles, respectively, in (c). The nodal line on $\Gamma - Z$ is highlighted by magenta. The transition point of band occupation are labeled by black dots in (d).

Figure 3. SHC and SNC in InBi. (a) and (b) Energy dependent SHC and SNC for the three independent tensor elements. (c) and (d) The evolution of SHC and SNC as the function of temperature. The solid curves and empty circles in (d) are from equation (4) and Mott relation, respectively.

tensor elements in InBi for both the SHC and SNC tensor [45–47], following the relation of $X^z_{xy} = -X^z_{yx}$, $X^y_{zx} = -X^x_{zy}$, and $X^x_{yz} = X^y_{xz}$ ($X = \sigma$ or α).

From the energy-dependent SHC (figure 3(a)), one can see that the largest tensor element appears at σ^z_{xy}, which can reach up to about 1100 $((\hbar/e)\,(\Omega\,cm)^{-1})$. Thus far, this is the only SHC above 1000 $((\hbar/e)\,(\Omega\,cm)^{-1})$ in the reported p-orbital compounds. This large value is robust in a large energy window from $E_0 - 0.5$ eV to the charge neutral points in the hole-doped range. Therefore, hole doping is preferred from the SHE point of view. Furthermore, the SHC is robust with respect to temperature. The SHC only varies less than 5% from 0 K to room temperature, which is very similar to that in platinum [16].

From the above model analysis, we already know that a large SHC does not imply a large SNC. To obtain a large SNC, the balance of the SHC distribution in energy space must be broken. Based on this understanding, the robustness of the SHC in energy space is not beneficial for the SNE, and a large SNC should not appear at α^z_{xy}. Indeed, the tensor element of α^z_{xy} is very small, at about 0.2 $((\hbar/e)(A/m \cdot K))$ at 300 K. However, a quite large SNC is achieved at α^y_{zx}, which can reach up to about 1.2$((\hbar/e)(A/m \cdot K))$ at

Table 1. SHC, SHA, SNC, and SNA for InBi and Pt at Fermi level and temperature 300 K. The unit for SHC and SNC are $(\hbar/e)(\Omega \cdot \text{cm})^{-1}$ and $((\hbar/e)(A/m \cdot K))$, respectively. (The data of Pt is taken from reference [16]).

		SHC	SHA	SNC	SNA
InBi	X_{xy}^z	1100	0.3	0.2	0.04
	X_{zx}^y	300	0.09	1.2	0.28
	X_{yz}^x	200	0.06	0.9	0.21
Pt	X_{xy}^z	2200	0.11	-3.0	-0.20

Table 2. Comparison of SNC from equation (2) and Mott relation. The unit is $((\hbar/e)(A/m \cdot K))$.

	10 K		100 K	
	equation (2)	Mott relation	equation (2)	Mott relation
α_{xy}^z	0.0	9.18×10^{-4}	9.18×10^{-3}	2.00×10^{-2}
α_{zx}^y	6.01×10^{-2}	2.96×10^{-2}	0.530	0.296
α_{yz}^x	4.02×10^{-2}	2.75×10^{-2}	0.361	0.275

300 K. Because the SNE is very sensitive to temperature, we also analyzed the evolution of the SNC as a function of temperature. As presented in figure 3(d), α_{xy}^z is near-zero at low temperatures below 100 K, and the α_{zx}^y and α_{yz}^x are also small ($\sim 0.5((\hbar/e)(A/m \cdot K))$). All three components increase steadily with temperature, but α_{zx}^y and α_{yz}^x increase much faster than α_{xy}^z. This is the reason why α_{xy}^z is so small even above 300 K.

For the conversion efficiency of the charge and heat current to the spin current not only the absolute values of the SHC and SNC are important, but also the SHA and the spin Nernst angle (SNA). In InBi [48], the SHA ($\theta_{\text{SH},xy}^z$) can reach up to 0.3 (see table 1), close to or even larger than that in the 5*d* transition metals of Pt, W, and Ta. Similarly, in combination with a large SNC and low thermal power, the SNA can reach up to 0.21 and 0.28 for $\theta_{\text{SN},yz}^x$ and $\theta_{\text{SN},zx}^y$, respectively.
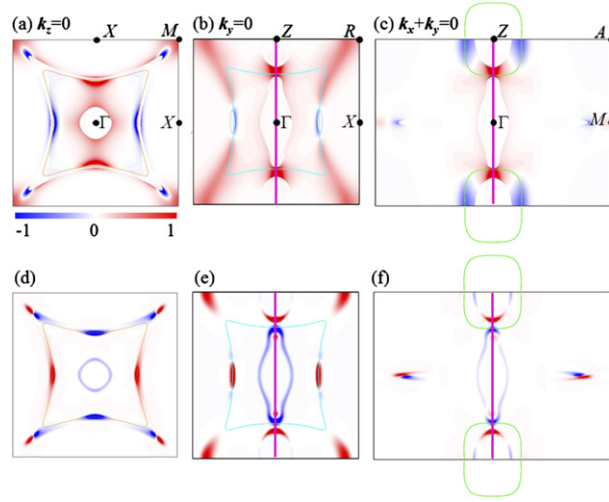
At low temperature, the SNC can be understood from the Mott relation [40, 49–51]:

$$\alpha_{ij}^k = -\frac{\pi^2}{3}\frac{k_B^2 T}{e}\frac{\partial \sigma_{ij}^k(E)}{\partial E} \tag{5}$$
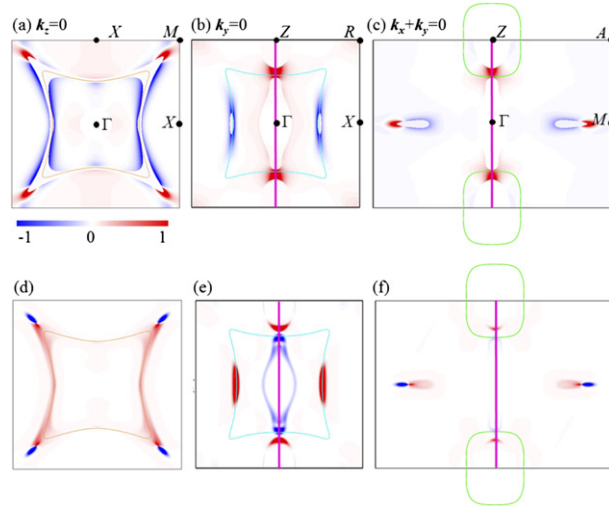
At a temperature of about 10 K, the SNC from both the Mott relation and SNBC formalism converge to about zero. From figure 3(c), one can easily see that the SNC from the different equations (2) and (3) agree very well with each other at low temperatures from 10 to 100 K. We also list the value from equations (2) and (3) in table 2.

From equations (1) and (2), one can see that the intrinsic SHC and SNC can be understood as the integral of the SBC and SNBC in the whole BZ. As the maximum elements are different for the SHC and SNC, we choose the SBC and SNBC from two different components of $\sigma(\alpha)_{xy}^z$ and $\sigma(\alpha)_{zx}^y$ to observe their distribution and temperature effect for the evolution from the SBC to SNBC. From the above band structure analysis, we know that the special band structures mainly focus on the high-symmetry planes of $k_{x,y} = 0$, $k_z = 0$, and $k_x \pm k_y = 0$, and high-symmetry line of Γ–Z. Therefore, we have analyzed the SBC and SNBC distribution in all the three planes of $k_{x,y} = 0$, $k_z = 0$, and $k_x + k_y = 0$.

First, we analyzed the component of $\Omega_{xy}^{\text{SNE},z}$, which contributes to the large tensor element for the SHC. As shown in figure 4(a), the large SBC in the $k_z = 0$ plane is mainly dominated by the Γ-centred nodal ring. In addition, there exist other hotspots on the Γ–M line near the M point, which is not exactly located on the nodal ring. This is because the SBC is indeed determined by the band structure with the SOC. The gapless linear crossing transforms to a anti-crossing by the SOC. Comparing the linear crossing point $K1$ (highlighted by orange circle) in figure 2(b) and the corresponding band anti-crossing point $K1'$ in figure 2(c), we can find that the $K1'$ is much closer to the M point than $K1$. Therefore, the hotspots along Γ–M do not exactly lie on the corner of the gapless nodal ring. Meanwhile, in the $k_y = 0$ plane, there are two types of hotspots, one from the nodal ring in the $k_y = 0$ plane and the other on the line Z–Γ–Z. The $\Omega_{xy}^{\text{SHE},z}$ from the nodal line on Z–Γ–Z is much larger, which is related to the magenta bands in figures 2(c) and (d). There are also two types of hotspots in the $k_x + k_y = 0$ plane, one from Z–Γ–Z as that in the $k_y = 0$ plane and the other from the Z-point-centred nodal ring. From figures 4(b) and (c), one can find some empty parts with a zero SBC and shape edge transition, such as the Γ- and Z-centred areas. This is due to the shape evolution of the band occupation, such as the band around the Γ point, as shown in

Figure 4. **Local Berry curvature $\Omega_{xy}^{\mathrm{SHE},z}(\vec{k})$ and $\Omega_{xy}^{\mathrm{SNE},z}(\vec{k})$ distribution on high symmetry planes** (a)–(c) and (d)–(f) are SBC and SNBC distribution on the three planes of $k_z = 0$, $k_y = 0$, and $k_x + k_y = 0$ planes, respectively. The nodal lines are also shown by orange, cyan, green circles, and magenta curves, respectively. The color bars are in arbitrary units.

Figure 5. **Local Berry curvature distribution on high symmetry planes for the component of $\Omega_{zx}^{\mathrm{SHE},y}(\vec{k})$ and $\Omega_{zx}^{\mathrm{SNE},y}(\vec{k})$** (a)–(c) and (d)–(f) are SBC and SNBC distribution on the three planes of $k_z = 0$, $k_y = 0$, and $k_x + k_y = 0$ planes, respectively. The nodal lines are also shown by orange, cyan, green circles, and magenta curves, respectively. The color bars are in arbitrary units.

figure 2(d). For the k point from R to Γ, the valence band changes from an occupied band to a non-occupied band after a transition k point (highlighted by the black dot). Similar behavior is also exhibited for the other areas with an empty SBC.

After taking the temperature effect into consideration, the SNBC ($\Omega_{xy}^{\mathrm{SNE},z}$) also mainly originates from the four classes of nodal lines as that for the SBC. The main difference is that the shape edge transitions in the empty SBC areas are replaced by the hotspot of the SNBC (see figures 4(d)–(f)). This is because the temperature effect smoothens considerably the transition of the band occupation, and the shape transition of the SBC around the edge of the empty area yields a large SNBC.

Similar to $\Omega_{xy}^{\mathrm{SHE},z}$, the component of $\Omega_{zx}^{\mathrm{SHE},y}$ is dominated by the four classes of nodal lines, but the volume of the negative part is larger than that of $\Omega_{xy}^{\mathrm{SHE},z}$, leading to a relatively smaller σ_{zx}^y. However, owing to the smaller negative $\Omega_{zx}^{\mathrm{SNE},y}$, α_{zx}^y is much larger than α_{xy}^z.

As the negative SNBC($\Omega_{zx}^{\mathrm{SNE},y}$) primarily originates from the sharp transition of the SBC around the edge of the zone with an empty SBC, the small magnitude of $\Omega_{zx}^{\mathrm{SHE},y}$ generates a relatively small SNBC for the same tensor component. Comparing figures 4 and 5, the Γ-centred negative hot rings for $\Omega_{xy}^{\mathrm{SNE},z}$ in figures 4(d) and (f) are almost invisible in figures 5(d) and (f) for $\Omega_{zx}^{\mathrm{SNE},y}$. Moreover, the Γ-centred negative hot ring for $\Omega_{zx}^{\mathrm{SNE},y}$ in figure 5(e) is also considerably weaker than $\Omega_{xy}^{\mathrm{SNE},z}$ in figure 5(d). Because both

components of α_{xy}^z and α_{zx}^y are positive values, the smaller negative $\Omega_{zx}^{\text{SNE},y}$ directly leads to a larger α_{zx}^y in comparison to α_{xy}^z.

In summary, from our calculations we predict a large SHC and SNC in the *p*-band semimetal InBi. Due to the contribution of the nodal lines in the band structure of InBi, the σ_{xy}^z component of the SHC can reach up to about 1100 $\left((\hbar/e)\,(\Omega\,\text{cm})^{-1}\right)$, the only SHC above 1000 $\left((\hbar/e)\,(\Omega\,\text{cm})^{-1}\right)$ in the reported *p*-band systems. In contrast to the intuition that a large SHC is always accompanied by a large SNC, the largest value for the SHC and SNC appear in a different element. The size of the SNC is mainly dependent on the breaking of the balance of the SHC distribution in energy space and gives the largest SNC of about $1.2((\hbar/e)(A/m\cdot K))$ at the tensor element α_{zx}^y, which is close to that in platinum. Since InBi is a semimetal with a low conductivity around $10^4(\Omega\,\text{cm})^{-1}$ even at 40 K [48], the extrinsic part from skew scattering would be suppressed, leaving the topological contribution as the dominant term. These results on InBi provide more general guiding principles to obtain a strong SHE and SNE in commercially more attractive *p*-band compounds and establishes a more comprehensive understanding of the relationship between the SHE and SNE in these materials.

Acknowledgments

ORCID iDs

Chenguang Fu ⓘ https://orcid.org/0000-0002-9545-3277

References

[1] Wolf S A, Awschalom D D, Buhrman R A, Daughton J M, Molnár S v, Roukes M L, Chtchelkanova A Y and Treger D M 2001 *Science* **294** 1488
[2] Zutic I, Fabian J and Sarma S 2004 *Rev. Mod. Phys.* **76** 323
[3] Bader S and Parkin S 2010 *Annu. Rev. Condens. Matter Phys.* **1** 71
[4] DYakonov M I and Perel V I 1971 *J. Exp. Theor. Phys.* **13** 467
[5] Hirsch J E 1999 *Phys. Rev. Lett.* **83** 1834
[6] Kato Y K, Myers R C, Gossard A C and Awschalom D D 2004 *Science* **306** 1910
[7] Sinova J, Valenzuela S O, Wunderlich J, Back C and Jungwirth T 2015 *Rev. Mod. Phys.* **87** 1213
[8] Valenzuela S O and Tinkham M 2006 *Nature* **442** 176
[9] Murakami S, Nagaosa N and Zhang S-C 2003 *Science* **301** 1348
[10] Sinova J, Culcer D, Niu Q, Sinitsyn N A, Jungwirth T and MacDonald A H 2004 *Phys. Rev. Lett.* **92** 126603
[11] Guo G, Yao Y and Niu Q 2005 *Phys. Rev. Lett.* **94** 226601
[12] Tanaka T, Kontani H, Naito M, Naito T, Hirashima D S, Yamada K and Inoue J 2008 *Phys. Rev. B* **77** 165117
[13] Hoffmann A 2013 *IEEE Trans. Magn.* **49** 5172
[14] Nagaosa N, Sinova J, Onoda S, MacDonald A H and Ong N P 2010 *Rev. Mod. Phys.* **82** 1539
[15] Xiao D, Chang M-C and Niu Q 2010 *Rev. Mod. Phys.* **82** 1959
[16] Meyer S *et al* 2017 *Nat. Mater.* **16** 977
[17] Sheng P, Sakuraba Y, Lau Y-C, Takahashi S, Mitani S and Hayashi M 2017 *Sci. Adv.* **3** e1701503
[18] Kim D-J, Jeon C-Y, Choi J-G, Lee J W, Surabhi S, Jeong J-R, Lee K-J and Park B-G 2017 *Nat. Commun.* **8** 1400
[19] Bernevig B A and Zhang S-C 2005 *Phys. Rev. Lett.* **95** 016801
[20] Cheng S, Xing Y, Sun Q-f and Xie X 2008 *Phys. Rev. B* **78** 045302
[21] Bauer G E W, Saitoh E and Wees B J v 2012 *Nat. Mater.* **11** 391
[22] Tauber K, Gradhand M, Fedorov D V and Mertig I 2012 *Phys. Rev. Lett.* **109** 026601
[23] Tauber K, Fedorov D V, Gradhand M and Mertig I 2013 *Phys. Rev. B* **87** 161114
[24] Wimmer S, Ködderitzsch D, Chadova K and Ebert H 2013 *Phys. Rev. B* **88** 201108
[25] Kimura T, Otani Y, Sato T, Takahashi S and Maekawa S 2007 *Phys. Rev. Lett.* **98** 156601
[26] Saitoh E, Ueda M, Miyajima H and Tatara G 2006 *Appl. Phys. Lett.* **88** 182509
[27] Mellnik A *et al* 2014 *Nature* **511** 449
[28] Han J, Richardella A, Siddiqui S A, Finley J, Samarth N and Liu L 2017 *Phys. Rev. Lett.* **119** 077702
[29] Mahendra D *et al* 2018 *Nat. Mater.* **17** 800
[30] Fan Y *et al* 2014 *Nat. Mater.* **13** 699
[31] Yasuda K, Tsukazaki A, Yoshimi R, Kondou K, Takahashi K, Otani Y, Kawasaki M and Tokura Y 2017 *Phys. Rev. Lett.* **119** 137204
[32] Wu H *et al* 2019 *Phys. Rev. Lett.* **123** 207205
[33] Khang N H D, Ueda Y and Hai P N 2018 *Nat. Mater.* **17** 808

[34] Chi Z, Lau Y-C, Xu X, Ohkubo T, Hono K and Hayashi M 2020 *Sci. Adv.* **6** eaay2324

[35] Sahin C and Flatte M E 2015 *Phys. Rev. Lett.* **114** 107201

[36] Fan J and Eom J 2008 *Appl. Phys. Lett.* **92** 142101

[37] Sun Y, Zhang Y, Felser C and Yan B 2016 *Phys. Rev. Lett.* **117** 146403

[38] Sun Y, Zhang Y, Liu C-X, Felser C and Yan B 2017 *Phys. Rev.* B **95** 235104

[39] Shi J, Zhang P, Xiao D and Niu Q 2006 *Phys. Rev. Lett.* **96** 076604 Note there is also a conserved spin current definition, which includes the spin-flip torque term

[40] Xiao D, Yao Y, Fang Z and Niu Q 2006 *Phys. Rev. Lett.* **97** 026603

[41] Guo G-Y and Wang T-C 2017 *Phys. Rev.* B **96** 224415

[42] Ekahana S A *et al* 2017 *New J. Phys.* **19** 065007

[43] Koepernik K and Eschrig H 1999 *Phys. Rev.* B **59** 1743

[44] Perdew J P, Burke K and Ernzerhof M 1996 *Phys. Rev. Lett.* **77** 3865

[45] Kleiner W H 1966 *Phys. Rev.* **142** 318

[46] Seemann M, Kodderitzsch D, Wimmer S and Ebert H 2015 *Phys. Rev.* B **92** 155138

[47] Zhang Y, Sun Y, Yang H, Železnỳ J, Parkin S P, Felser C and Yan B 2017 *Phys. Rev.* B **95** 075128

[48] Cooper G, Saunders G and Lawson A 1964 *J. Phys. Chem. Solids* **25** 1277 Due to the lack of experimental values for the electrical conductivity and thermopower of InBi film, we have just used the bulk values to estimate the SHA and SNA. It should be noted that the conductivity and thermalpower in bulk is normally much larger than that in film form, which would lead an even larger SHA and SNA in thin film. The conductivity in *xy* plane is isotropic because of four fold rotation symmetry around *z* axis. Note that the reported conductivity in this reference does not specify the lattice direction, which might induces some difference for the estimation of SHA and SNA

[49] Lee W-L, Watauchi S, Miller V L, Cava R J and Ong N P 2004 *Phys. Rev. Lett.* **93** 226601

[50] Xiao C, Zhu J, Xiong B and Niu Q 2018 *Phys. Rev.* B **98** 081401

[51] Dong L, Xiao C, Xiong B and Niu Q 2020 *Phys. Rev. Lett.* **124** 066601